

Observation of exceptional points and realization of high sensitivity sensing in electric circuits

Jiaxi Cai(蔡家希), Xinyi Wang(王鑫怡), Xiaomin Zhang(张晓敏), Taoran Yue(乐陶然), and Jijun Wang(王纪俊)
Citation: Chin. Phys. B, 2025, 34 (**12**): 128402. DOI: 10.1088/1674-1056/adec5e
http://cpb.iphy.ac.cn; http://iopscience.iop.org/cpb

What follows is a list of articles you may be interested in

Simulation of the non-Hermitian Kitaev chain by electrical circuits

Jiali Xu(徐佳莉), Hao Geng(耿昊), Abdul Wahab, Xiaosen Yang(杨孝森), Yuee Xie(谢月娥), and Yuanping Chen(陈元平)
Chin. Phys. B, 2025, 34 (**6**): 068401. DOI: 10.1088/1674-1056/adbedb

Reconfigurable Mott electronics for homogeneous neuromorphic platform

Zhen Yang(杨振), Ying-Ming Lu(路英明), and Yu-Chao Yang(杨玉超)
Chin. Phys. B, 2023, 32 (**12**): 128401. DOI: 10.1088/1674-1056/ad02e8

Observation of size-dependent boundary effects in non-Hermitian electric circuits

Luhong Su(苏鹭红), Cui-Xian Guo(郭翠仙), Yongliang Wang(王永良), Li Li(李力), Xinhui Ruan(阮馨慧), Yanjing Du(杜燕京), Shu Chen(陈澍), and Dongning Zheng(郑东宁)
Chin. Phys. B, 2023, 32 (**3**): 038401. DOI: 10.1088/1674-1056/aca9c4

A review on the design of ternary logic circuits

Xiao-Yuan Wang(王晓媛), Chuan-Tao Dong(董传涛), Zhi-Ru Wu(吴志茹), and Zhi-Qun Cheng(程知群)
Chin. Phys. B, 2021, 30 (**12**): 128402. DOI: 10.1088/1674-1056/ac248b

Suppression of ferroresonance using passive memristor emulator

S Poornima
Chin. Phys. B, 2021, 30 (**6**): 068401. DOI: 10.1088/1674-1056/abd7e0

Observation of exceptional points and realization of high sensitivity sensing in electric circuits

Jiaxi Cai(蔡家希)[1], Xinyi Wang(王鑫怡)[2], Xiaomin Zhang(张晓敏)[1], Taoran Yue(乐陶然)[1], and Jijun Wang(王纪俊)[1,†]

[1] *School of Physics and Electronic Engineering, Jiangsu University, Zhenjiang* 212013, *China*
[2] *School of Electrical and Information Engineering, Jiangsu University, Zhenjiang* 212013, *China*

(Received 28 May 2025; revised manuscript received 3 July 2025; accepted manuscript online 7 July 2025)

We explore the parity-time (PT)-symmetry breaking transition in a dimer circuit composed of two RLC resonators that are weakly coupled via an inductor. The energy behavior of this dimer circuit is reflected in the splitting or degeneracy of the systems eigenfrequencies as the gain–loss strength varies. Its dynamical properties can be described by a non-Hermitian Hamiltonian. The eigenfrequency spectrum of the system is divided by two critical points into three distinct regions: the symmetric region, the oscillatory growth region, and the fully exponential growth region. Building upon previous work on implementing the exceptional point (EP) in circuit systems, our study focuses on further exploring the variation patterns of circuit eigenfrequencies near the EP under weak coupling conditions. In addition, we construct a corresponding Dirac point (DP) circuit system for comparison. By leveraging the unique physical properties near both the EP and the DP, we further propose potential practical applications. Using perturbation theory and system simulations, we demonstrate that the square-root eigenfrequency splitting near the EP significantly enhances the sensitivity to small external perturbations, compared to the linear splitting behavior near the DP. This study presents promising prospects for next-generation sensing technologies.

Keywords: parity-time symmetry, exceptional point, Dirac point, high sensitivity sensor

PACS: 84.30.–r, 03.65.vf, 03.65.Ta, 07.07.Df

DOI: 10.1088/1674-1056/adec5e **CSTR:** 32038.14.CPB.adec5e

1. Introduction

In recent years, non-Hermitian systems have gradually become a research hotspot owing to their unique physical properties.[1–11] This interest originally stemmed from the pioneering work of Carl Bender and his colleagues,[12,13] and rapidly expanded after they first applied the theory to the optical domain.[14–18] Among the various physical phenomena in non-Hermitian parity-time (PT)-symmetric systems, EP stands out as the most significant, attracting considerable attention for their enhanced sensing capabilities and potential to achieve energy-efficient transport.[19–33]

An EP is a degeneracy in a non-Hermitian system that exhibits unique properties, fundamentally different from the degeneracies in conventional Hermitian systems. At an EP, not only do two or more eigenvalues coalesce, but more importantly, their corresponding eigenstates also become degenerate, rendering the Hamiltonian matrix non-diagonalizable.[34] This simultaneous coalescence of eigenvalues and eigenstates is a distinctive feature of non-Hermitian systems.

It is worth noting that although non-Hermitian systems have been observed across a wide range of platforms, including optical,[35,36] acoustics,[37–41] cold atoms[42–44] and mechanical systems,[45–48] electronic circuits offer distinct advantages over these platforms, such as highly tunable design, manipulation, and detection capabilities. These features make electronic circuits a powerful platform for realizing various topological phases.[49–59] Through simple circuit designs, novel models can be constructed to simulate quantum phenomena such as topological condensed matter states, providing a suitable experimental platform for exploring unique physical phenomenon in non-Hermitian systems, including PT-symmetry breaking, resonance, and scattering. Furthermore, owing to the strong applicability of electronic circuits, the physical properties of these systems can be used to develop novel practical applications.[60]

EP sensors operate by tuning the working point of the system in parameter space to a position close to an EP, enabling a significantly amplified response to small perturbations. Compared to conventional Dirac point (DP) sensors, EP sensors offer much higher sensitivity. It is important to emphasize that, for sensors, sensitivity is a broad concept that includes both the responsivity of the sensing system and its signal-to-noise ratio (SNR).[61] Although EP-based sensors can significantly enhance the responsivity of the sensing system, the SNR does not exhibit a substantial improvement compared to conventional sensing systems.[62,63] Near an EP, the eigenfrequency splitting follows a square-root dependence on the perturbation strength,[64] which implies that even ex-

†Corresponding author. E-mail: wjj4461@ujs.edu.cn

© 2025 Chinese Physical Society and IOP Publishing Ltd. All rights, including for text and data mining, AI training, and similar technologies, are reserved.

tremely small disturbances can induce substantial frequency shifts, allowing for the detection of weak signals with high amplification.[65] In addition, EP sensors possess rich multifunctionality. Due to the diverse physical phenomena present in non-Hermitian systems, such as mode coupling, abrupt phase transitions, and unidirectional reflectionlessness.[66] EP sensors are highly suitable for a wide range of applications. These include metrology and sensing,[32,67–70] topological energy transfer,[71] polarization state conversion,[72] and on-chip photonic devices such as optical isolators[73,74] and directional lasers.[75]

In this work, we experimentally realize the frequency symmetry-breaking phenomenon in a weakly inductively coupled PT-symmetric dimer circuit system, and subsequently construct a corresponding DP circuit system. The physical properties of the DP circuit are also experimentally verified. Based on the distinct physical characteristics of the two circuit systems, we compare the sensitivity of the EP and DP systems under identical perturbation strengths. The comparison leads us to conclude that the EP-based sensing system exhibits significantly higher sensitivity to external perturbations than the conventional DP-based sensing system. Our research provides an efficient solution for next-generation sensing technologies in various fields, such as food safety and hygiene detection,[76–87] crop growth monitoring,[88] and photoelectrochemical biosensing detection.[89]

The structure of this paper is as follows. In Section 2, we present the inductively coupled PT-symmetric dimer model and its corresponding dynamical equations described by a non-Hermitian Hamiltonian, along with a brief analysis of its fundamental physical properties. The analysis of circuit frequency modes near the EP and the DP under different gain–loss strength, along with experimental data, is provided in Sections 3 and 4. In Section 5, we demonstrate the frequency splitting behaviors and sensitivity near the EP and DP based on perturbation theory and simulation. Finally, in Section 6, we present an overall conclusion that summarizes our research findings.

2. Theoretical analysis of the dimer model

The experimental circuit platform we designed is illustrated in Fig. 1. It consists of an RLC oscillator with loss and a corresponding RLC oscillator with gain, coupled via mutual inductance M. The loss side incorporates a positive resistor R1 to introduce dissipation, while the gain side employs a negative resistor R2, realized using an operational amplifier with a gain factor of two. Voltage measurements at the two nodes V_1 and V_2 are conducted using voltage buffers. The coupled eigenfrequencies of this system exhibit PT-symmetry-breaking transitions. In practical sensing applications, the inductive coils gradually approach each other under applied pressure, leading to an increase in the coupling coefficient. This variation results in a shift in the voltage response frequency, enabling pressure sensing. This circuit structure not only provides an intuitive demonstration of symmetry breaking in non-Hermitian PT-symmetric systems, but also enables the observation of amplified responses to external perturbations through appropriate circuit design, thus achieving high sensitivity sensing. To investigate the dynamical properties of the PT-symmetric circuit and establish the non-Hermitian Hamiltonian that describes the system, we first disregard the signal source and the matching impedance Z. We then perform

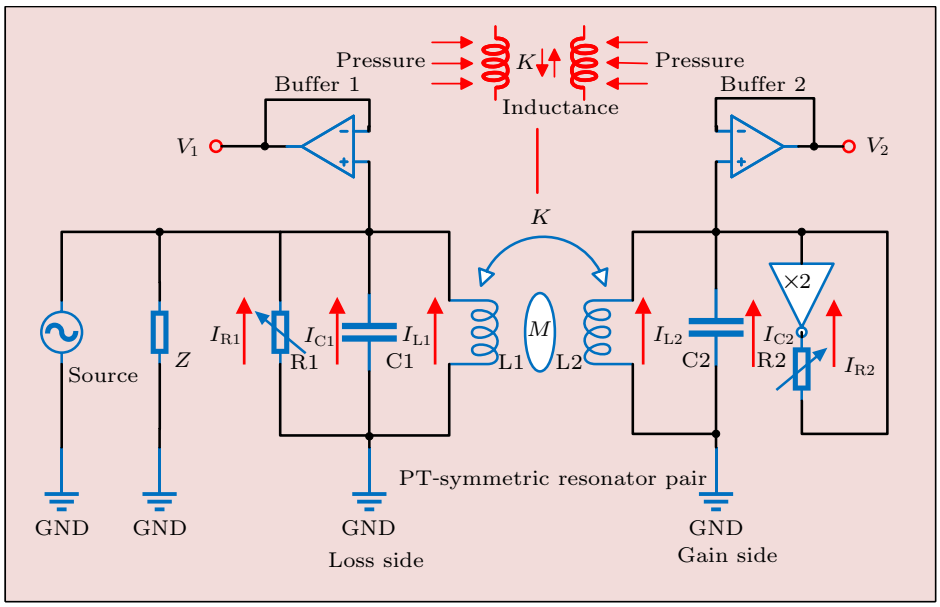


Fig. 1. Schematic of the PT-symmetric dimer circuit and its potential sensing platform configuration. The circuit system consists of two inductively coupled RLC resonators that respectively provide gain and loss, forming a PT-symmetric sensing circuit when connected in parallel with a matching impedance Z and a signal source.

loop analysis on the two probing nodes V_1 and V_2 of the circuit over the time interval from 0 to t. By applying Kirchhoff laws, we obtain the following equations for the two nodes:

$$I_{R1}+I_{C1}+I_{L1}=0, \tag{1}$$

$$I_{R2}+I_{C2}+I_{L2}=0, \tag{2}$$

$$V_1=-I_{R1}\cdot R_1=-\frac{1}{C}\cdot\int_0^t I_{C1}(\tau)\,\mathrm{d}\tau, \tag{3}$$

$$V_2=I_{R2}\cdot R_2=-\frac{1}{C}\cdot\int_0^t I_{C2}(\tau)\,\mathrm{d}\tau, \tag{4}$$

$$V_1=-L\cdot\frac{\mathrm{d}I_{L1}}{\mathrm{d}t}-M\cdot\frac{\mathrm{d}I_{L2}}{\mathrm{d}t}, \tag{5}$$

$$V_2=-L\cdot\frac{\mathrm{d}I_{L2}}{\mathrm{d}t}-M\cdot\frac{\mathrm{d}I_{L1}}{\mathrm{d}t}. \tag{6}$$

To facilitate the formulation of the non-Hermitian Hamiltonian, we define the normalized time constant as $\tau=\omega_0\cdot t$, where $\omega_0=1/\sqrt{LC}$ is the resonance frequency of the LC resonators. The gain–loss strength of the PT-symmetric circuit system is given by $\gamma=\sqrt{L/C}/R$, and the coupling coefficient between the left and right circuit branches is defined as $\mu=M/L$. According to Eqs. (2)–(6), it is straightforward to verify that under the combined operations of parity ($V_1\leftrightarrow V_2$) and time reversal ($t\leftrightarrow -t$), the equations remain invariant. Therefore, the circuit system satisfies PT symmetry. These equations can be reformulated as a set of four linearly coupled differential equations:

$$\frac{\mathrm{d}V_1}{\mathrm{d}t}=-\gamma\omega_0 V_1+\frac{I_{L1}}{C}, \tag{7}$$

$$\frac{\mathrm{d}V_2}{\mathrm{d}t}=\gamma\omega_0 V_2+\frac{I_{L2}}{C}, \tag{8}$$

$$\frac{\mathrm{d}I_{L1}}{\mathrm{d}t}=\frac{-V_1+\mu V_2}{L(1-\mu^2)}, \tag{9}$$

$$\frac{\mathrm{d}I_{L2}}{\mathrm{d}t}=\frac{-V_2+\mu V_1}{L(1-\mu^2)}. \tag{10}$$

Next, we derive the Hamiltonian that governs the dynamical behavior of this circuit system. To this end, we construct a column vector $\psi=[V_1,V_2,I_{L1},I_{L2}]^{\mathrm{T}}$, and rewrite Eqs. (7)–(10) in the form of a Schrödinger-like equation

$$\mathrm{i}\frac{\mathrm{d}\psi}{\mathrm{d}t}=\begin{bmatrix}-\mathrm{i}\gamma\omega_0 & 0 & \mathrm{i}\gamma R\omega_0 & 0\\ 0 & \mathrm{i}\gamma\omega_0 & 0 & \mathrm{i}\gamma R\omega_0\\ \frac{-\mathrm{i}\omega_0}{\gamma R(1-\mu^2)} & \frac{\mathrm{i}\mu\omega_0}{\gamma R(1-\mu^2)} & 0 & 0\\ \frac{\mathrm{i}\mu\omega_0}{\gamma R(1-\mu^2)} & \frac{-\mathrm{i}\omega_0}{\gamma R(1-\mu^2)} & 0 & 0\end{bmatrix}\psi=H_{\mathrm{EP}}\psi. \tag{11}$$

The fourth-order matrix in Eq. (11) is the Hamiltonian matrix H_{EP}, which characterizes the dynamical properties of the circuit system. In such a system, the eigenfrequencies are crucial physical quantities that reflect the operational state of the circuit. We will solve for the eigenvalues of the Hamiltonian matrix based on Eq. (12) in order to investigate the eigenfrequency characteristics of the PT-symmetric circuit under different parameter conditions:

$$\mathrm{Det}\,|H_{\mathrm{EP}}-I\cdot\omega|=0. \tag{12}$$

Here, matrix I denotes the identity matrix of order n, which in Eq. (12) is taken to be a fourth-order identity matrix. Thus, the eigenfrequencies of the system are obtained as follows:

$$\omega_{1,2}=\frac{W_0}{2}\sqrt{\frac{2+2\sqrt{1-\mu^2}}{1-\mu^2}-\gamma^2}\pm\sqrt{\frac{2-2\sqrt{1-\mu^2}}{1-\mu^2}-\gamma^2}, \tag{13}$$

$$\omega_{3,4}=-\frac{W_0}{2}\sqrt{\frac{2+2\sqrt{1-\mu^2}}{1-\mu^2}-\gamma^2}\pm\sqrt{\frac{2-2\sqrt{1-\mu^2}}{1-\mu^2}-\gamma^2}. \tag{14}$$

It can be observed that under different parameter settings, both pairs of eigenfrequencies exist in complex conjugate forms. By appropriately selecting the parameters μ and γ, the system can be tuned to operate at the EP. The selected parameters are as follows:

$$\mu_{\mathrm{EP}}=0.45,\quad \gamma_{\mathrm{EP}}=0.52. \tag{15}$$

To further investigate the physical properties of the system, we present the phase diagram in the two-dimensional parameter space, as shown in Fig. 2.

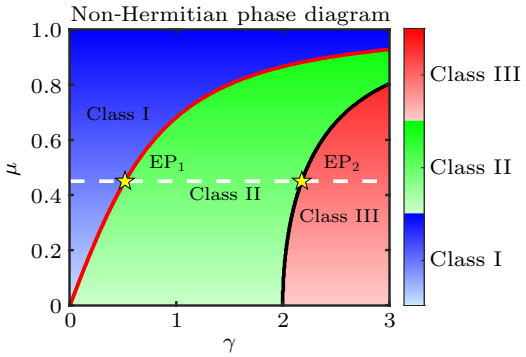


Fig. 2. Phase diagram of the EP circuit system in the two-dimensional parameter space of μ and γ. The blue, green, and red regions represent class I, II, and III exceptional point formation patterns (EPFPs), respectively, which are separated by red and black solid lines. Each class represents a distinct EPFP. The white dashed line represents the trajectory of our EP circuit system, where the parameter μ is fixed while γ is varied to obtain two EPs. The locations of the two EPs are marked with yellow pentagrams.

It can be seen that, in our EP system, the parameters are set by fixing $\mu=0.45$ and varying the system parameter γ. As γ gradually increases, the system transitions from class I to class II,[90] during which the first exceptional point (EP_1) emerges. With further increase in γ, the system then transitions from class II to class III, leading to the emergence of the second exceptional point (EP_2). Specifically, the class I region corresponds to the oscillatory behavior of the system voltage;

the class II region corresponds to the oscillatory growth behavior; and the class III region corresponds to purely exponential growth of the voltage. In this work, we focus on investigating the physical properties near EP_1 and, based on this, propose a sensing circuit application scheme.

Figure 3 shows the three-dimensional and two-dimensional band diagrams of the system in the μ and γ parameter space. For the EP system, we take a cut of the three-dimensional band diagram at $\mu = 0.45$ to obtain the two-dimensional band diagram. It can be seen that, under the parameter selection in Eq. (15), the system's eigenfrequencies undergo a second-order degeneracy. As the gain–loss strength γ increases, the eigenfrequencies of the system acquire imaginary components. With a further increase in γ, all eigenfrequencies of the system become purely imaginary. We will fix the coupling coefficient of the circuit system at $\mu = 0.45$ and gradually increase the value of γ, measuring whether the system's eigenfrequencies at different γ values match the theoretical frequency shifts near the EP.

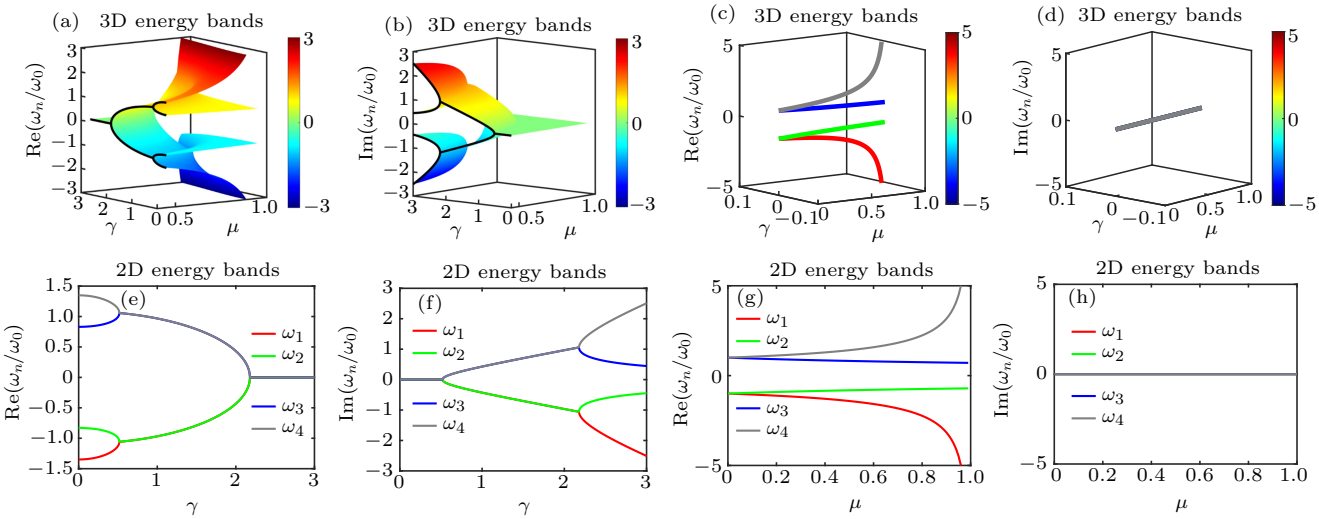


Fig. 3. Three-dimensional and two-dimensional band structures of EP and DP systems in the parameter space. ω_1, ω_2, ω_3, and ω_4 denote the eigenenergies of the two systems. (a) Real part of the three-dimensional energy band structure of the EP circuit system. (b) Imaginary part of the three-dimensional energy band structure of the EP circuit system. (c) Real part of the three-dimensional energy band structure of the DP circuit system. (d) Imaginary part of the three-dimensional energy band structure of the DP circuit system. (e), (f) Real and imaginary parts of the two-dimensional energy band structure of the EP system for a fixed parameter μ. (g), (h) Real and imaginary parts of the two-dimensional energy band structure of the DP system.

In the Hermitian limit ($\gamma = 0$), our system transitions from EP to DP. For the DP system, as the coupling coefficient μ increases, the system's eigenfrequencies gradually split from the resonance frequency of the LC circuit into a low-frequency and a high-frequency branch. We will gradually increase the coupling coefficient μ and measure whether the system's eigenfrequencies at different μ values align with the theoretical frequency shifts near the DP. The band diagrams in Fig. 3 provide the theoretical foundation for our subsequent simulations and experimental work.

3. Frequency change of PT symmetric circuit

3.1. EP system

To further investigate the working principle of this PT-symmetric dimer circuit, we will use the simulation software Advanced Design System (ADS) to simulate the circuit system. We will obtain time-domain waveforms for different gain–loss strength, then perform fast Fourier transform (FFT) on the time-domain waveforms to convert them into frequency-domain waveforms, thus obtaining the eigenfrequencies for different γ values. Through the ADS simulation, we find that the waveforms at the two nodes, V_1 and V_2, in the circuit system have the same frequency, with only the voltage amplitudes differing. Therefore, we will only display the typical waveforms at the V_2 node in three parameter regions, as shown in Fig. 4.

For the EP system, we obtain waveforms for different values of the parameter γ that include three regions. As shown in Figs. 4(a) and 4(e), first is class I, where the time-domain waveform is the superposition of two sinusoidal signals with different frequencies. As shown in Figs. 4(c) and 4(g), next is class II, where the time-domain waveform is the superposition of a sinusoidal signal with a specific frequency and an exponentially growing signal. As shown in Figs. 4(d) and 4(h), finally is class III, where the time-domain waveform consists only of an exponentially growing voltage signal. As shown in Figs. 4(b) and 4(f), the boundary between class I and the class II is the second-order EP. At the EP, the circuit's eigenfrequencies $\omega_{1,2}$ and $\omega_{3,4}$ coincide, leading to the second-order EP. At this point, the eigenfrequency of the circuit system is the frequency contributed by the EP.

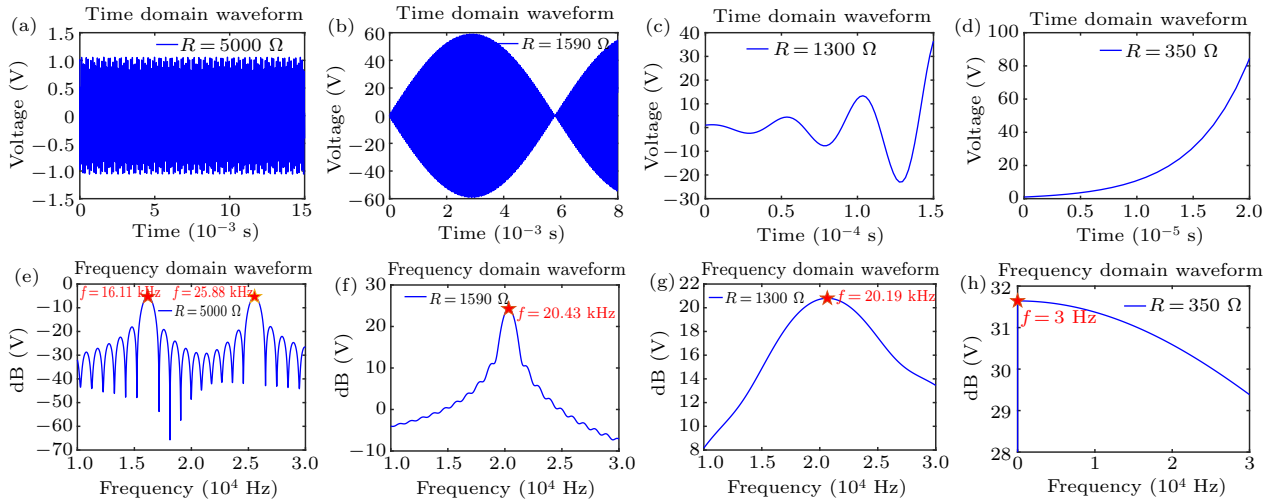


Fig. 4. Time domain and frequency domain waveform diagrams of the EP circuit system with a fixed coupling coefficient of $\mu = 0.45$ in different intervals. (a), (e) Time domain and frequency domain waveforms within the PT-symmetric interval. (b), (f) Time domain and frequency domain waveforms at the EP. (c), (g) Time domain and frequency domain waveforms within the PT-symmetry breaking interval. (d), (h) Time domain and frequency domain waveforms within the complete exponential growth interval.

3.2. DP system

Our circuit design also supports the realization of the DP circuit system. For the DP system, we observe two modes of waveforms. As shown in Figs. 5(a) and 5(c), the first mode consists of a sine wave voltage signal at the LC coil resonance frequency, corresponding to the second-order DP of the system. As shown in Figs. 5(b) and 5(d), the second mode is a mixed waveform containing two frequencies. As the inductive coupling coefficient increases, the two frequency modes gradually separate from each other. The resonance frequency contributed by the LC coil decreases at a slower rate, while the frequency contributed by the change of coupling coefficient increases at a faster rate.

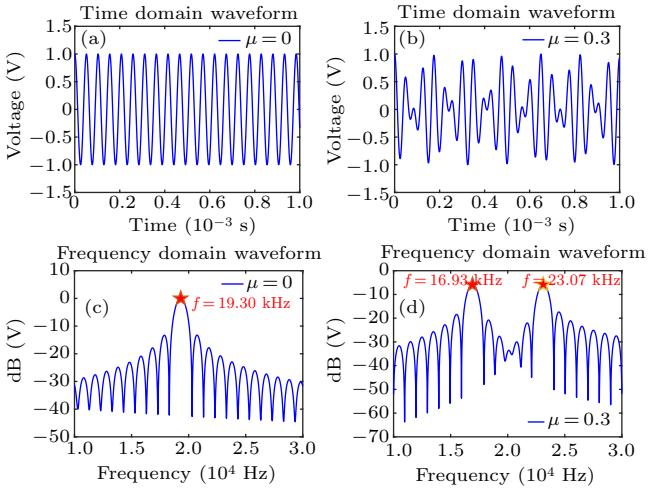


Fig. 5. Time domain and frequency domain waveforms of the DP circuit system with different coupling coefficients. (a) and (c) Time domain and frequency domain waveforms at the DP. (b) and (d) Time domain and frequency domain waveforms away from the DP.

4. Experimental setup and results

In the PT-symmetric circuit breaking transition experiment, for the EP system, we fixed the coupling coefficient of the inductors on both sides and varied the values of the positive and negative resistors on each side to change the system's gain–loss coefficient γ. This allowed us to observe changes in the circuit's time-domain waveform. We then used the FFT function of the oscilloscope to measure and obtain the system's eigenfrequencies.

To precisely adjust the resistance values of the left and right positive and negative resistors and visualize them, we will use a programmable resistor module instead of the common potentiometer. It is important to note that as the γ value gradually increases, meaning the positive and negative resistors on both sides gradually decrease, the system first enters the PT-symmetric region. Then, as the γ value increases, the system passes through the EP and enters the symmetry-breaking region, eventually reaching the fully oscillatory growth region. When the circuit system operates in the latter two regimes, the frequency components include exponentially growing modes, causing the voltage to increase exponentially. This poses challenges for our experiments. Therefore, we adopted an alternative but equivalent approach: using a signal generator as the input source, with the voltage amplitude set to 1 V and the frequency tuned to the fundamental frequency of the LC circuit. This setup enables us to better observe the frequency response of the PT-symmetric dimer circuit. To avoid FFT data distortion caused by the voltage range limitations of the oscilloscope, we analyze the voltage waveform measured by the oscilloscope over the time interval from 0 to 0.16 ms. In the DP system, we adjust the coupling strength by changing the distance between the two inductors on either side, and analyze the voltage waveform within the time interval from 0 to 1 ms. When using the oscilloscope's frequency spectrum analysis function, to prevent low-frequency and high-frequency noise generated by the system and environment from affecting subsequent measurements,[91]

we need to set the digital filter for the channel under test to bandpass filter mode. Finally, we compare the measured eigenfrequency data with the theoretical and simulation data, and as shown in Figs. 6(a) and 6(b), all three match very well. Figures 7(a) and 7(b) show the top-view PCB layouts of the EP and DP systems, while Figs. 7(c) and 7(d) present their corresponding experimental platform setups.

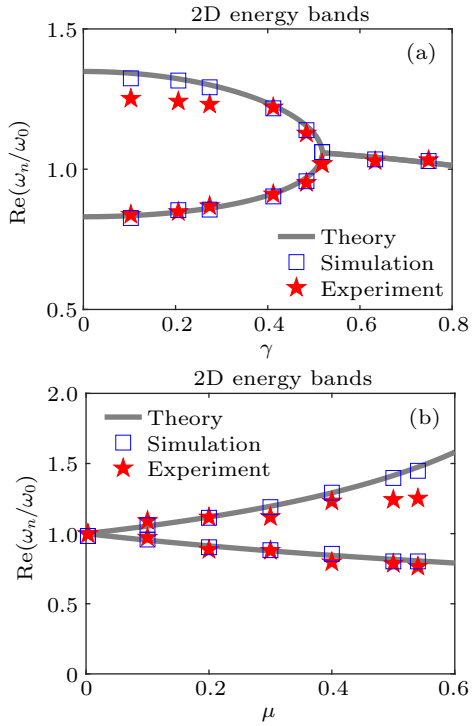


Fig. 6. The 2D band diagrams of EP and DP systems, with the line representing theoretical predictions, squares representing simulation results, and stars representing experimental data. (a) Theoretical, simulation, and experimental results for the EP system. (b) Theoretical, simulation, and experimental results for the DP system.

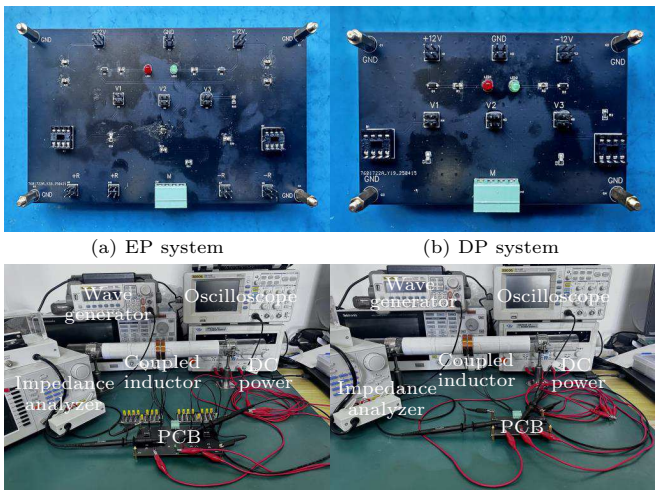


Fig. 7. Experimental platform and PCB top view.

5. PT symmetrical sensing circuit

In the previous sections, we have verified the existence of second-order EP and DP in our circuit system through theoretical analysis, simulations, and experiments. Next, we will investigate the sensitivity of the system under external perturbations. In our system, perturbations can occur in any component of the RLC circuit structure, i.e., by varying either μ or γ in the two-dimensional parameter space. However, in practical scenarios, changing the parameter γ requires simultaneously adjusting both the positive and negative resistances. Negative resistance implemented using operational amplifiers is highly sensitive to feedback resistor values, and it is challenging to achieve simultaneous and precise adjustments of both positive and negative resistances under external perturbations. To align with practical sensor circuit designs, we ultimately consider using perturbations to vary the parameter μ, thereby shifting the circuit system away from the EP. Another advantage of this design is that the coupled inductors can serve as platforms for detecting various physical quantities such as pressure, velocity, and temperature, endowing our system with multi-parameter sensing capabilities.

After determining that the perturbation acts on the inductors L to alter the coupling coefficient, we use the ADS simulation software to simulate this perturbation. In our system, changes in the coupling coefficient of the two inductors affect the overall impedance of the system, which in turn directly influences the transmission properties of the entire sensing circuit. The minimum point of the S_{11} parameter of the sensing circuit corresponds to the impedance matching condition, indicating minimal return loss at that point. We can determine the frequency variation of the sensing circuit under different perturbation strengths by comparing the frequency values corresponding to the minimum of the reflection coefficient.[92,93]

When configuring the circuit system in the simulation software, all component parameters are kept consistent with those used in the study of PT-symmetric circuit phase transitions, except for the coupling coefficient between the two inductors, which is varied through a parameter sweep. Additionally, our circuit includes a signal source and a matching impedance Z, as shown in Fig. 1. This readout design ensures that the entire sensing network remains impedance-matched with the internal impedance of the signal generator near the EP, thereby avoiding reflection of backward-propagating waves into the generator.[94] Next, an S-parameter simulator and a parameter sweep controller are added to the simulation circuit. The S-parameter simulator is used to measure the S_{11} parameter of the sensing circuit, while the parameter sweep controller performs a stepwise scan of the perturbation strength applied to the coupling coefficient between the two inductors. The perturbation strength ξ is set to range from 0 to 0.1 to simulate the variation in the S_{11} parameter of the circuit under weak perturbation.

Next, we will theoretically analyze the dependence of the S_{11} parameter on small perturbations ξ by performing a se-

ries expansion of the eigenfrequencies near the EP and DP. It is important to note that due to the degeneracy of eigenstates at the EP, the traditional Taylor series expansion is no longer applicable and should be replaced by the Puiseux series. For our system, the series expansions at the EP and DP yield the following conclusions:

$$\delta\omega_{\mathrm{EP}} = 0.42\xi^{\frac{1}{2}} + 0.22\xi^{1} + 0.23\xi^{\frac{3}{2}} + o(\xi^{2}) + \cdots, \quad (16)$$

$$\delta\omega_{\mathrm{DP}} = \frac{1}{2}\xi^{1} + \frac{3}{8}\xi^{2} + \frac{5}{16}\xi^{3} + o(\xi^{4}) + \cdots. \quad (17)$$

As shown in Figs. 8(a) and 8(b), when the perturbation ξ is 0, both the EP and DP systems operate exactly at the second-order EP and DP, respectively, and there is only one resonance frequency in the reflection coefficient spectrum. As the perturbation strength ξ gradually increases, the entire sensing circuit system deviates from both the second-order EP and DP, leading to the emergence of another resonance frequency that shifts to the right. We extract the shifts in these resonance frequencies, denoted as $\delta\omega$, and present them in Fig. 8(c).

When analyzing Eqs. (16) and (17), we focus only on the lower-order terms in the series expansions that have the dominant influence on the results, i.e., we truncate the expansions to the first-order terms. From Fig. 8(c), we observe that the eigenfrequency shift near the EP is proportional to $\xi^{1/2}$, whereas near the DP it is proportional to ξ^{1}, which is in perfect agreement with our theoretical predictions. Among the existing methods for defining the sensitivity of sensing circuits,[31,61] our approach is similar to that used for calculating eigenfrequency shifts. We adopt the widely accepted term responsivity to characterize and represent the amplification of the detected signal, using it to describe the sensing systems response precision to external perturbations as part of the overall sensitivity characterization of the system. Specifically, we define the responsivity of EP and DP systems as the first-order derivative of the eigenfrequency shift $\delta\omega$ with respect to the perturbation strength ξ. The expression for the responsivity S is given by

$$S = \frac{\partial\delta\omega}{\partial\xi}. \quad (18)$$

As shown in Fig. 7(d), under the same external perturbation strength, the frequency shift in the EP system is significantly larger than that in the DP system, thus achieving a higher perturbation responsivity.

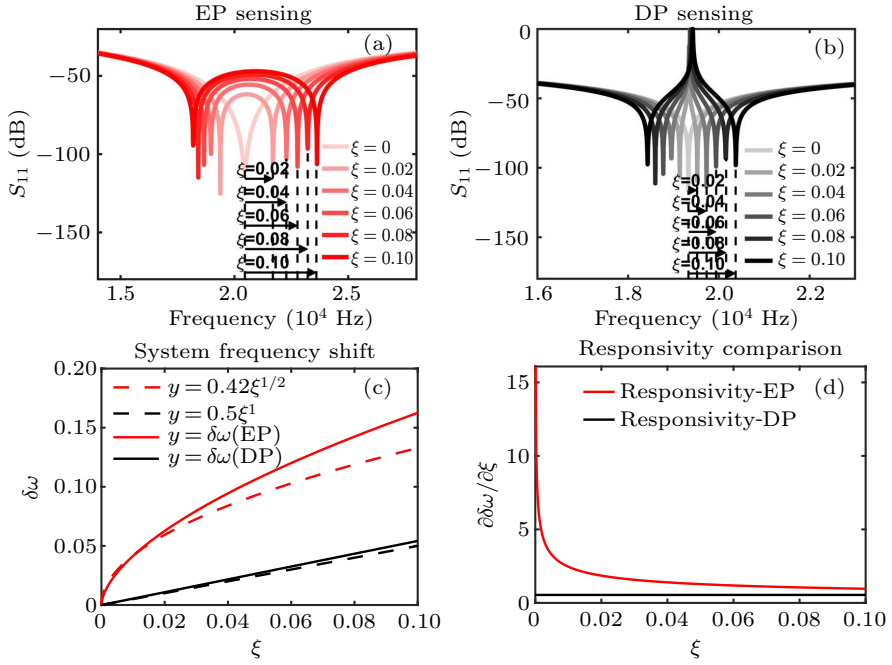


Fig. 8. Reflection coefficient and responsivity near the EP and DP. (a) Magnitude of the S_{11} reflection coefficient for the EP sensing system under different perturbation strengths. (b) Magnitude of the S_{11} reflection coefficient for the DP sensing system. (c) Eigenfrequency shifts at EP and DP; the dashed line indicates the expression of the corresponding series expansion truncated at first order. (d) Comparison of responsivity at EP and DP. Component values are chosen as follows: $L = 6.78$ mH, $C = 10$ nF, $R = 1590\ \Omega$, $Z = 50\ \Omega$. For the EP sensing system, $\mu = 0.45$; for the DP system, $\mu = 0$.

6. Conclusions

In this work, we present the theoretical analysis, simulations, experimental realization, and potential applications of PT symmetry in electronic circuit systems. First, we introduce the basic structure of a PT-symmetric circuit dimer. Unlike previous work, our dimer circuit operates under weak coupling conditions and employs a coupling inductor as the foundation for a sensing platform. The weak coupling regime is more feasible in practical scenarios, and the tunability of the coupling strength via the inductor offers flexibility for future sensing circuit designs. Subsequently, through circuit simulations and experiments, we obtain eigenfrequency variation plots that are

consistent with theoretical predictions and simulations. Our work also provides the theoretical derivation, simulation results, and experimental verification of a corresponding DP circuit system. Based on the distinct frequency characteristics near the EP and DP, we propose circuit sensing designs utilizing both regimes. Finally, by applying perturbation theory and performing both simulation and measurement of the S_{11} parameters near the EP and DP, we provide stronger evidence compared to previous studies that the responsivity at the EP is significantly higher than that at the DP, highlighting the substantial advantage of EP-based systems in sensing applications. Although numerous studies have demonstrated that the responsivity is greatly enhanced at the EP, the SNR of the system does not show a corresponding improvement. To simultaneously enhance the SNR of EP-based sensing systems, recent works have proposed utilizing the transmission peak degeneracy effect to achieve a threefold increase in SNR.[92] Alternatively, randomly generated EPs in sensors can benefit from environmental noise through stochastic resonance, thereby improving the SNR.[95] These approaches enable EP sensors to achieve higher precision and robustness.

By tuning the circuits operating parameters and structural topology to reside near the EP, the PT-symmetric system leverages its singularity to achieve sensing sensitivities far exceeding those of conventional techniques, while also enabling efficient, stable wireless power transfer. Our results promise to accelerate the maturation of emerging applications, such as ultra-high-sensitivity optical sensors,[96] precision parameter detection,[97] and near-lossless energy transmission[98] and thus have opened new avenues for integrating actual electrical devices with advanced circuit architectures.

Acknowledgement

We gratefully acknowledge the financial support of the Natural Science Foundation of Jiangsu Province (Grant No. BK20231320).

References

[1] Lee T E 2016 *Phys. Rev. Lett.* **116** 133903
[2] Yao S and Wang Z 2018 *Phys. Rev. Lett.* **121** 086803
[3] Longhi S 2019 *Phys. Rev. Lett.* **122** 237601
[4] Pan L, Chen X, Chen Y and Zhai H 2020 *Nat. Phys.* **16** 767
[5] Cao Y, Li Y and Yang X 2021 *Phys. Rev. B* **103** 075126
[6] Wang J H, Tao Y L and Xu Y 2022 *Chin. Phys. Lett.* **39** 010301
[7] Yang X, Cao Y and Zhai Y 2022 *Chin. Phys. B* **31** 010308
[8] Li Y, Ji X, Chen Y, Yan X and Yang X 2022 *Phys. Rev. B* **106** 195425
[9] Li Y, Cao Y, Chen Y and Yang X 2022 *J. Phys.: Condens. Matter* **35** 055401
[10] Zhang Y X, Zhang Z T, Yang Z S, Wei X Z and Liang B L 2024 *Chin. Phys. B* **33** 060308
[11] Zhang S M, He T Y and Jin L 2024 *Chin. Phys. Lett.* **41** 027201
[12] Bender C M and Boettcher S 1998 *Phys. Rev. Lett.* **80** 5243
[13] Bender C M 2007 *Reports on Progress in Physics* **70** 947
[14] Guo A, Salamo G J, Duchesne D, Morandotti R, Volatier-Ravat M, Aimez V, Siviloglou G A and Christodoulides D N 2009 *Phys. Rev. Lett.* **103** 093902
[15] Rüter C E, Makris K G, El-Ganainy R, Christodoulides D N, Segev M and Kip D 2010 *Nat. Phys.* **6** 192
[16] Ji X, Ding W, Chen Y and Yang X 2024 *Phys. Rev. B* **109** 125420
[17] Ji X and Yang X 2024 *J. Phys.: Condens. Matter* **36** 243001
[18] Ji X, Geng H, Akhtar N and Yang X 2025 *Phys. Rev. B* **111** 195419
[19] El-Ganainy R, Makris K G, Christodoulides D N and Musslimani Z H 2007 *Opt. Lett.* **32** 2632
[20] Schindler J, Li A, Zheng M C, Ellis F M and Kottos T 2011 *Phys. Rev. A* **84** 040101
[21] Schindler J, Lin Z, Lee J M, Ramezani H, Ellis F M and Kottos T 2012 *J. Phys. A: Math. Theor.* **45** 444029
[22] Lin Z, Schindler J, Ellis F M and Kottos T 2012 *Phys. Rev. A* **85** 050101
[23] Ge L, Chong Y D and Stone A D 2012 *Phys. Rev. A* **85** 023802
[24] Wiersig J 2014 *Phys. Rev. Lett.* **112** 203901
[25] Sounas D L, Fleury R and Alù A 2015 *Phys. Rev. Appl.* **4** 014005
[26] Fleury R, Sounas D and Alù A 2015 *Nat. Commun.* **6** 5905
[27] Doppler J, Mailybaev A A, Böhm J, Kuhl U, Girschik A, Libisch F, Milburn T J, Rabl P, Moiseyev N and Rotter S 2016 *Nature* **537** 76
[28] Wiersig J 2016 *Phys. Rev. A* **93** 033809
[29] Assawaworrarit S, Yu X and Fan S 2017 *Nature* **546** 387
[30] Chen W, Kaya Özdemir Ş, Zhao G, Wiersig J and Yang L 2017 *Nature* **548** 192
[31] Xiao Z, Li H, Kottos T and Alù A 2019 *Phys. Rev. Lett.* **123** 213901
[32] Dong Z, Li Z, Yang F, Qiu C W and Ho J S 2019 *Nat. Electron.* **2** 335
[33] Assawaworrarit S and Fan S 2020 *Nat. Electron.* **3** 273
[34] Ding K, Fang C and Ma G 2022 *Nat. Rev. Phys.* **4** 745
[35] Wang C, Fu Z, Mao W, Qie J, Stone A D and Yang L 2023 *Advances in Optics and Photonics* **15** 442
[36] Johnston A and Berloff N G 2024 *Phys. Rev. Lett.* **132** 096901
[37] Gao H, Xue H, Gu Z, Liu T, Zhu J and Zhang B 2021 *Nat. Commun.* **12** 1888
[38] Gu Z, Gao H, Cao P C, Liu T, Zhu X F and Zhu J 2021 *Phys. Rev. Appl.* **16** 057001
[39] Xue H, Yang Y and Zhang B 2022 *Nat. Rev. Mater.* **7** 974
[40] Zhang Q, Zhao L, Liu X, Feng X, Xiong L, Wu W and Qiu C 2023 *Phys. Rev. Res.* **5** L022050
[41] Liu C, Lan J, Gu Z and Zhu J 2023 *Chin. Phys. Lett.* **40** 124301
[42] Li L, Lee C H and Gong J 2020 *Phys. Rev. Lett.* **124** 250402
[43] Zhou L, Li H, Yi W and Cui X 2022 *Commun. Phys.* **5** 252
[44] Liu D, Ren Z, Wong W C, Zhao E, He C, Pak K K, Jo G B and Li J 2024 *Phys. Rev. A* **109** 053305
[45] Brandenbourger M, Locsin X, Lerner E and Coulais C 2019 *Nat. Commun.* **10** 4608
[46] Yoshida T and Hatsugai Y 2019 *Phys. Rev. B* **100** 054109
[47] Chen Y, Li X, Scheibner C, Vitelli V and Huang G 2021 *Nat. Commun.* **12** 5935
[48] Cui X, Zhang R Y, Wang X, Wang W, Ma G and Chan C T 2023 *Phys. Rev. Lett.* **131** 237201
[49] Ningyuan J, Owens C, Sommer A, Schuster D and Simon J 2015 *Phys. Rev. X* **5** 021031
[50] Albert V V, Glazman L I and Jiang L 2015 *Phys. Rev. Lett.* **114** 173902
[51] Helbig T, Hofmann T, Lee C H, Thomale R, Imhof S, Molenkamp L W and Kiessling T 2019 *Phys. Rev. B* **99** 161114
[52] Bao J, Zou D, Zhang W, He W, Sun H and Zhang X 2019 *Phys. Rev. B* **100** 201406
[53] Wang H, Ruan J and Zhang H 2019 *Phys. Rev. B* **99** 075130
[54] Hofmann T, Helbig T, Lee C H, Greiter M and Thomale R 2019 *Phys. Rev. Lett.* **122** 247702
[55] Yu R, Zhao Y X and Schnyder A P 2020 *National Science Review* **7** 1288
[56] Zhang X X and Franz M 2020 *Phys. Rev. Lett.* **124** 046401
[57] Ghorashi S A A, Li T and Sato M 2021 *Phys. Rev. B* **104** L161117
[58] Yu L W and Deng D L 2021 *Phys. Rev. Lett.* **126** 240402
[59] Su L, Guo C X, Wang Y, Li L, Ruan X, Du Y, Chen S and Zheng D 2023 *Chin. Phys. B* **32** 038401
[60] Yang H, Song L, Cao Y and Yan P 2024 *Phys. Rep.* **1093** 1
[61] Langbein W 2018 *Phys. Rev. A* **98** 023805

[62] Zhang M, Sweeney W, Hsu C W, Yang L, Stone A D and Jiang L 2019 *Phys. Rev. Lett.* **123** 180501
[63] Wang H, Lai Y H, Yuan Z, Suh M G and Vahala K 2020 *Nat. Commun.* **11** 1610
[64] Hodaei H, Hassan A U, Wittek S, Garcia-Gracia H, El-Ganainy R, Christodoulides D N and Khajavikhan M 2017 *Nature* **548** 187
[65] Sakhdari M, Hajizadegan M, Zhong Q, Christodoulides D N, El-Ganainy R and Chen P Y 2019 *Phys. Rev. Lett.* **123** 193901
[66] Wang C, Rao J, Chen Z, Zhao K, Sun L, Yao B, Yu T, Wang Y P and Lu W 2024 *Nat. Phys.* **20** 1139
[67] Lau H K and Clerk A A 2018 *Nat. Commun.* **9** 4320
[68] Bai K, Peng Z, Luo H G and An J H 2019 *Phys. Rev. Lett.* **123** 040402
[69] Budich J C and Bergholtz E J 2020 *Phys. Rev. Lett.* **125** 180403
[70] Bai K, Luo H G, Zhang W and Xiao M 2020 *Phys. Rev. A* **101** 022115
[71] Xu H, Mason D, Jiang L and Harris J G E 2016 *Nature* **537** 80
[72] Hassan A U, Zhen B, Soljačić M, Khajavikhan M and Christodoulides D N 2017 *Phys. Rev. Lett.* **118** 093002
[73] Choi Y, Hahn C, Yoon J W, Song S H and Berini P 2017 *Nat. Commun.* **8** 14154
[74] Zhang X L, Jiang T and Chan C T 2019 *Light: Science & Applications* **8** 88
[75] Peng B, Özdemir Ş K, Liertzer M, Chen W, Kramer J, Yılmaz H, Wiersig J, Rotter S and Yang L 2016 *Proc. Natl. Acad. Sci. USA* **113** 6845
[76] Xu Y, Zhang W, Shi J, Li Z, Huang X, Zou X, Tan W, Zhang X, Hu X, Wang X and Liu C 2020 *Food Chemistry* **322** 126762
[77] Yin L, You T, El-Seedi H R, El-Garawani I M, Guo Z, Zou X and Cai J 2022 *Food Chemistry* **396** 133707
[78] Adade S Y S S, Lin H, Haruna S A, Barimah A O, Jiang H, Agyekum A A, Johnson N A N, Zhu A, Ekumah J N, Li H and Chen Q 2022 *Journal of Food Composition and Analysis* **114** 104834
[79] Wang L, Haruna S A, Ahmad W, Wu J, Chen Q and Ouyang Q 2022 *Food Chemistry* **388** 132950
[80] Kang W, Lin H, Yao-Say Solomon Adade S, Wang Z, Ouyang Q and Chen Q 2023 *Food Chemistry* **405** 134193
[81] Li H, Bei Q, Zhang W, Marimuthu M, Hassan M M, Haruna S A and Chen Q 2023 *Food Chemistry* **422** 136202
[82] Ding X, Ahmad W, Wu J, Rong Y, Ouyang Q and Chen Q 2023 *Food Chemistry* **404** 134761
[83] Wu H, Xie R, Hao Y, Pang J, Gao H, Qu F, Tian M, Guo C, Mao B and Chai F 2023 *Food Chemistry* **418** 135961
[84] Lai J, Ding L, Liu Y, Fan C, You F, Wei J, Qian J and Wang K 2023 *Food Chemistry* **423** 136285
[85] Zhou M, Dai C, Aheto J H and Zhang X 2024 *Journal of Food Safety* **44** e13163
[86] Li H, Murugesan A, Shoaib M, Sheng W and Chen Q 2024 *Critical Reviews in Food Science and Nutrition* pp. 1–33
[87] Adade S Y S S, Lin H, Johnson N A N, Nunekpeku X, Aheto J H, Ekumah J N, Kwadzokpui B A, Teye E, Ahmad W and Chen Q 2025 *Trends in Food Science & Technology* **156** 104851
[88] Liu N, Zhang W, Liu F, Zhang M, Du C, Sun C, Cao J, Ji S and Sun H 2022 *Agronomy* **12** 2139
[89] Mao H, Du X, Yan Y, Zhang X, Ma G, Wang Y, Liu Y, Wang B, Yang X and Shi Q 2022 *International Journal of Agricultural and Biological Engineering* **15** 180
[90] Ding K, Ma G, Xiao M, Zhang Z Q and Chan C T 2016 *Phys. Rev. X* **6** 021007
[91] Zhou Y, Wang H Y, Wang L F, Dong L and Huang Q A 2023 *Journal of Physics Communications* **7** 065003
[92] Kononchuk R, Cai J, Ellis F, Thevamaran R and Kottos T 2022 *Nature* **607** 697
[93] Yin K, Hao X, Huang Y, Zou J, Ma X and Dong T 2023 *Phys. Rev. Appl.* **20** L021003
[94] Pozar D M 2021 *Microwave Engineering: Theory and Techniques* (John Wiley & Sons)
[95] Li Z, Li C, Xiong Z, Xu G, Wang Y R, Tian X, Yang X, Liu Z, Zeng Q, Lin R, Li Y, Lee J K W, Ho J S and Qiu C W 2023 *Phys. Rev. Lett.* **130** 227201
[96] Mao W, Fu Z, Li Y, Li F and Yang L 2024 *Science Advances* **10** eadl5037
[97] Yuan H, Zhang W, Zhou Z, Wang W, Pan N, Feng Y, Sun H and Zhang X 2023 *Advanced Science* **10** 2301128
[98] Li Z Z and Whaley K B 2024 *Phys. Rev. Res.* **6** 023149